Journal of Materials Chemistry A

ROYAL SOCIETY OF CHEMISTRY

PAPER

View Article Online
View Journal | View Issue

Cite this: J. Mater. Chem. A, 2024, 12, 28177

Impact of Cu^+ and Cu^{2+} species on the oxide-metal transition processes of Cu_xO foams during the CO_2RR probed by *operando* Quick-XAS†

S. Blaseio, [a] C. Dosche, [b] M. Rahaman, [cd] K. Kiran, [ce] A. Dworzak, [a] B. Mahrt, [a] P. Broekmann, [c] A. Dutta *[c] and M. Oezaslan *[a]

As a promising electrocatalyst for the CO_2 reduction reaction (CO_2RR), Cu/Cu oxide (Cu_xO) derived materials have been intensively studied in the last few decades. However, it is still poorly understood how the structure of Cu/Cu_xO precursors and their simultaneous reduction process influence CO_2RR product distribution. Using Quick X-ray absorption near edge structure spectroscopy (Quick-XANES), we aim to understand the potential-dependent reduction processes of Cu_xO foam precursors with different Cu^0 : Cu^+ : Cu^{2+} ratios to pure metallic Cu during the CO_2RR. Initially, the Cu_xO foams were prepared by thermal annealing of electrodeposited Cu foams at 100, 200, 300, and 450 °C in air to vary the Cu^0 : Cu^+ : Cu^{2+} ratio and especially the crystallinity of CuO. With these different chemical states and structures, the oxide-metal transition kinetics during the cathodic potential increment (ΔE = 100 mV), step (ΔE >100 mV), and jump (ΔE >500 mV) experiments were comprehensively investigated using multivariate curve resolution-alternating least squares (MCR-ALS) analysis of the Quick-XANES data. This allows in *operando* monitoring of the changes in the chemical state of Cu species particularly in relation to the effect of the previously applied potential. In principle, two rate determining steps can be involved in the CuO reduction to Cu^0 *via* intermediate Cu^+ formation. First, our results demonstrate that the oxide-metal transition kinetics strongly depend on the initial abundance of Cu^{2+} species and precursor structure (ordered *vs.* amorphous) as well as on the type of chronoamperometric experiment. More precisely, compared to amorphous CuO, a high initial population of crystalline CuO species leads to a significant shift of the oxide-metal transition potential towards lower cathodic values, signifying a lower energy barrier to reduction. In addition, our work reveals that the different chronoamperometric experiments strongly influence the electrochemical stability of Cu^+ species within the Cu_xO foams during CO_2 electrolysis. Smaller potential steps increase the formation of Cu^+ species and lead to a slowdown in the reduction kinetics.

Received 2nd April 2024
Accepted 13th September 2024

DOI: 10.1039/d4ta02217c

rsc.li/materials-a

1. Introduction

In consideration of the still increasing CO_2 emissions, there is a high demand to directly convert CO_2 into valuable products, such as hydrocarbons as fuels and/or basic chemicals such as CO, formic acid, or alcohols for industrial applications. The electrochemically produced syngas can then be transformed into products of higher values by *e.g.* Fischer–Tropsch synthesis or biotechnological transformations.[1] As a promising alternative to fossil resources, the electrochemical CO_2 reduction reaction (CO_2RR) is being increasingly investigated for use in the large-scale production of hydrocarbons.[2–4] However, there are still challenges left including the very poor solubility of CO_2 in water, leading to sluggish kinetics, poor product selectivity, highly complex multiple-step reaction mechanisms with various intermediates, the hydrogen evolution reaction (HER) as a competing reaction, poor understanding of the influence of the reaction conditions such as pH as well as the type of electrolyte and the structure of active catalyst species are still under discussion.[2–5] Several electrode materials were investigated by Hori *et al.* and only copper is able to form hydrocarbons in sufficient quantities.[6] Not only the electrode material determines the resulting CO_2RR products, but also the

[a]Technical Electrocatalysis Laboratory, Institute of Technical Chemistry, Technische Universität Braunschweig, Franz-Liszt-Str. 35a, 38106 Braunschweig, Germany. E-mail: m.oezaslan@tu-braunschweig.de

[b]Institute of Chemistry, University of Oldenburg, Carl-von-Ossietzky-Str. 9-11, 26129 Oldenburg, Germany

[c]Department of Chemistry, Biochemistry and Pharmaceutical Sciences, University of Bern, Freiestr. 3, 3012 Bern, Switzerland. E-mail: abhijit.dutta@unibe.ch

[d]Yusuf Hamied Department of Chemistry, University of Cambridge, Lensfield Road, Cambridge CB2 1EW, UK

[e]Forschungszentrum Jülich GmbH, Institute of Energy and Climate Research, Wilhelm-Johnen-Str., 52428 Jülich, Germany

† Electronic supplementary information (ESI) available. See DOI: https://doi.org/10.1039/d4ta02217c

morphological characteristics such as shape, size and composition strongly influence product distribution.[7–9] In addition, partial or complete surface oxidation of nanostructured copper is used to enhance the electrochemically active surface area and create more active surface sites required for selective CO_2RR.[10,11] Common synthesis methods to generate these Cu oxide-derived catalysts include anodization, electro-polishing and cathodic electrodeposition.[7,10,12–15] These methods are usually followed by either thermal annealing, chemical oxidation, or oxygen plasma treatment to generate thin Cu_2O/CuO surface layers.[4,7,12,16–20] Bulk oxide formation is usually disfavored since it can lead to a reduced electrical conductivity and can result in kinetic stabilization of the oxide phases within the catalyst even at highly reductive potentials.[14] Usually, the Cu oxides (CuO and Cu_2O) formed during the oxidation step are thermodynamically unstable at potentials typically applied during the CO_2RR.[21] Therefore, the electrochemical reduction during the CO_2RR generates *in situ* oxide-derived (OD) Cu catalysts.[4] Interestingly, Cavalca *et al.* proposed that subsurface oxygen, present even under CO_2RR conditions in a 1–2 nm amorphous copper layer, is being responsible for enhanced CO adsorption on the OD-Cu surface.[22,23] However, DFT calculations by Fields *et al.* indicate that no subsurface oxygen will remain thermodynamically stable under highly cathodic conditions and are thus unlikely the reason for enhanced activity of OD-Cu catalysts.[24] A recent Raman and DFT study by Zhan *et al.* showed that the surface of Cu_2O nanoparticles was reduced to Cu^0 before the CO_2RR sets in and revealed that the extent of CO surface coverage determines the efficiency of C–C coupling.[25] Altogether, the stability of subsurface oxygen is still controversially and intensively discussed in the literature.[4,24–26]

Most investigations were focused on the influence of the oxidic precursor on the CO_2RR product distribution, faradaic efficiencies and surface structure changes.[4] As an example, Valesco-Vélez *et al.* studied Cu oxidation state changes during the CO_2RR in CO_2-saturated 0.1 M $KHCO_3$.[27] For Cu^+, a reduction to Cu^0 was found at -0.8 $V_{Ag/AgCl}$ $\approx$ -0.2 V_{RHE} (3.4 M KCl).[27] However, for pure CuO foam, no reduction occurred over the entire potential range up to -0.8 V_{RHE} due to the formation of a stable copper carbonate layer at the surface. This passivation suppressed the cathodic reduction of CuO to metallic Cu and Cu_2O.[27] Timoshenko *et al.* and Jeon *et al.* showed that by time-resolved LCA-XANES analysis at -1.0 V_{RHE} and -0.7 V_{RHE} the successive reduction of mainly Cu^+ containing Cu nanocubes and nanocrystals can be studied in detail, but no conclusions on the influence of the different Cu species on the reduction processes were made.[28,29] The above mentioned examples show that the specific role of the oxides as well as the transition process to Cu^0 in the active catalysts for the CO_2RR are not fully understood and so far no general conclusion has been achieved in the literature.[14,19,20,22–25,30–34]

With this work, we aim to understand the influence of the $Cu^0 : Cu^+ : Cu^{2+}$ ratio on the kinetics of the electrochemical oxide to metal reduction process of in air annealed Cu_xO foams during the CO_2RR. The samples were prepared by the recently developed hydrogen-assisted electrodeposition of Cu as foam-type materials.[7,14,30,35] As described in the literature, partial or complete surface oxidation of the copper is achieved by thermal annealing in air.[16,17,30] These electrodeposition and thermal annealing steps increase the electrochemically active surface area for electrodeposited samples as well as create the active sites on the Cu_xO foam surface, which are required for highly selective CO_2RR.[10] To generate different $Cu^0 : Cu^+ : Cu^{2+}$ ratios, the foams were annealed in air at four different temperatures ranging from 100–450 °C. For studying time- and potential-resolved changes of the chemical state of Cu species in the Cu_xO foams during the CO_2RR, we applied *operando* (Quick) X-ray absorption spectroscopy (XAS).

To understand the transition processes of the cupric and cuprous to metallic Cu species, we investigated the influence of chronoamperometric protocols by applying small potential steps ($\Delta E = 100$ mV) and large cathodic potential jumps ($\Delta E >$ 500 mV). To the knowledge of the authors, most studies in the literature used potential increment type of experiments, where only small potential shifts were applied to the Cu-based catalyst material.[14,26,27,36,37] However, our study showed that different electrochemical protocols have a substantial impact on the oxide-metal transition process.

2. Experimental

2.1. Chemicals

For the preparation of solutions $CuSO_4 \cdot 5H_2O$ (Sigma-Aldrich, ACS grade), H_2SO_4 (Sigma-Aldrich, ACS grade), $KHCO_3$ (Sigma-Aldrich, ACS grade) and Milli-Q water (Millipore, 18.2 MΩ cm, 4 ppb of total organic carbon) were used without further purification.

2.2. Cu_xO foam preparation

Cu_xO foams were prepared by electrodeposition onto activated carbon foil substrates (0.25 mm thick, 99.8%, Alfa Aesar, Germany) using the dynamic hydrogen bubble template approach.[7,10,38,39] The carbon foil substrates were activated by a thermal treatment at 550 °C for 12 h in air, followed by rinsing in an acetone/water mixture (1 : 1 volume ratio) and subsequent drying at 100 °C for 1 h. For electrodeposition the carbon foil with a geometric surface area of 1 cm^2 was exposed to a Cu plating bath containing 0.2 M $CuSO_4 \cdot 5H_2O$ and 1.5 M H_2SO_4. As a counter electrode a Cu plate (5 cm × 5 cm) and as the reference an Ag/AgCl (3 M KCl, Metrohm) electrode were used. The galvanostatic deposition process was carried out for 5 s at a current density of -3.0 A cm^{-2} normalized by the geometric electrode surface area. Afterwards, all Cu foam samples were thoroughly dried in an Ar flow (99.999%, Carbagas, Switzerland) followed by the thermal annealing treatment in a tube furnace (GERO GmbH, Germany) at temperatures of 100 °C, 200 °C, 300 °C or 450 °C for 12 h in air, respectively.

2.3. *Ex situ* characterization of the annealed Cu_xO foams

The structure and morphology of annealed foams were evaluated by using a Zeiss Gemini 450 scanning electron microscope equipped with an InLens secondary electron detector and a back-scattering detector. An accelerating voltage of 5 kV and currents of 75 pA were applied at a working distance of 5 mm. A

Bruker D8 X-ray diffractometer was operated at 40 mA and 40 kV with Cu Kα radiation (1.540 Å) and a scan rate of 0.1° min^{-1} to obtain crystal information of annealed Cu_xO foams. The XRD profiles were analyzed with the TOPAS software (Bruker, Version 5). An ESCALAB 250 Xi X-ray photoelectron spectrometer (Thermo Fisher) equipped with a monochromatic Al Kα X-ray source (1486.6 eV) was used to determine the chemical state of Cu surface species of annealed foams. Experimental parameters for the acquisition of survey and high-resolution XPS spectra of C 1s, O 1s and Cu 2p as well as Auger spectra of Cu LMM are summarized in Table S1 in the ESI.† The XPS and Auger data were analyzed using Avantage software (version 5.9952). Raman spectra of the annealed Cu_xO foams were acquired using a WITec alpha300 RSA confocal microscope using an excitation wavelength of 532 nm with a laser power of 1 mW, a 600 l mm^{-1} grating and a Zeiss EC Epiplan-Neofluar Dic 50×/0.8 NA objective.

2.4. CO_2RR electrolysis

The CO_2 electrolysis experiments were conducted using a custom-built, airtight glass cell (H-type). The three-electrode setup included a leakless Ag/AgCl (3 M KCl) reference electrode (EDAQ), Pt foil (15 mm × 5 mm) as a counter electrode, and the graphite-supported annealed Cu_xO foam catalysts (5 s deposition time at −3.0 A cm^{-2}) as the working electrodes. To evaluate any chloride ion contamination in the working electrolyte solution from the Ag/AgCl (3 M KCl) reference electrode, ion exchange chromatography (IC) was employed, with a detection limit of 100 ppb Cl anions. Before starting electrolysis, both the cathodic and anodic compartments were filled with 30 mL of 0.5 M $KHCO_3$ electrolyte solution (ACS grade, Sigma Aldrich) and were saturated with CO_2 gas (99.999%, Carbagas, Switzerland). The catholyte and anolyte were separated using a polymer membrane (Nafion 117, Sigma Aldrich). The potentiostatic CO_2 electrolysis was performed using a potentiostat (Metrohm Autolab 302N, The Netherlands), while the current interrupt method (Autolab Nova) was utilized to determine and compensate for the *iR* drop.

For CO_2RR product analysis, the headspace gas from the catholyte compartment was vented with CO_2, allowing the gaseous electrolysis products to be transferred into the gas sampling loop of the gas chromatograph (GC 8610C, SRI Instruments). The GC was equipped with a packed Hayesep D column and FS-INNOPEG 2000 column for separating the gaseous and non-volatile (alcohols) products respectively. Argon (99.9999%, Carba Gas) served as the carrier gas. For quantifying all gaseous CO_2 reduction reaction (CO_2RR) products, a flame ionization detector (FID) coupled to a methanizer was used, while hydrogen was quantified using a thermal conductivity detector (TCD).

The partial current density for each gaseous electrolysis product was calculated using the following equation:

$$I(\mathrm{i}) = X_\mathrm{i} \cdot n_\mathrm{i} \cdot F \cdot V_\mathrm{m}$$

where X_i is the volume fraction of the product i measured *via* online GC using a calibration gas mixture in Ar (Carbagas, Switzerland), n_i is the number of electrons involved in forming the product i, V_m is the molar CO_2 gas flow rate and F is the Faraday constant. The partial current density of each product was normalized to the total current density, providing the faradaic efficiency (FE, %) for each product. Gas samples were analyzed every 20 minutes during steady-state CO_2 electrolysis. Non-volatile alcohols were measured using a second FID detector (without methanizer). After electrolysis, an aliquot of the electrolyte was injected into the FS-INNOPEG 2000 column using a microliter syringe. Non-volatile ionic liquid products, such as formate, that could accumulate in the catholyte electrolyte during CO_2 electrolysis were analyzed using ion exchange chromatography coupled with a conductivity detector. The setup included a Metrohm Advanced Modular Ion Chromatograph with an L-7100 pump and a Metrosep A Supp 7-250 column.

2.5. Cu K-edge Quick-XAS data acquisition and analysis

Quick-XAS data recorded at the Cu K-edge was obtained at the SuperXAS (X10DA) beamline of Swiss Light Source (SLS), Switzerland. The storage ring was operated with a beam current of 400 mA and an energy of 2.4 GeV. A fast oscillating channel cut crystal monochromator allowed recording one spectrum in 1 s. The ionization chambers for the detection of the incident and transmitted X-ray radiation were filled with N_2. For background subtraction and edge step normalization of the XAS spectra, the ProXAS software suite[40] was used. The normalized data was analyzed using the MCR-ALS GUI 2.0 MatLab script, performing multivariate curve resolution-alternating least squares (MCR-ALS) on the Quick-XANES data.[41–43] In addition, conversion of the energy units (eV) to photon electron wave factor k units ($Å^{-1}$) was carried out using the ATHENA software (version: 0.9.26).[44] The resulting $\chi(k)$ functions were weighted with k^2 to account for the dampening of the XAS amplitude with increasing k. Using Fourier-transformation, the extended X-ray absorption fine structure (EXAFS) spectra were transformed to obtain pseudo radial structure functions (RSFs). For EXAFS analysis the amplitude reduction factor ($S_0{}^2$) was determined from Cu foil to be 0.89. The coordination number (N), interatomic bond length (R), mean squared bond length disorder (σ^2), and correction to the energy origin (ΔE_0), together with the error bars, were established for Cu–Cu and Cu–O scattering pairs by fitting the theoretical EXAFS signals to the data in R-space using the ARTEMIS software[44] (version: 0.9.26). *Ex situ* XAS data of the reference materials (Cu foil, Cu_2O and CuO) and thermally annealed Cu_xO foams were collected every second for 6–10 min and subsequently averaged. Powder materials (Cu_2O and CuO) were mixed with a binder (cellulose) and measured as a pellet. The IFEFF6 data for EXAFS fitting analysis were determined from Cu (#9008468), Cu_2O (#1010963) and CuO (#9008961) taken from the crystal open database (COD).[45–47]

2.6. *Operando* Quick-XAS conditions

A home-made spectro-electrochemical flow cell was used, which consisted of a three-electrode configuration based on the basic design published by Binninger *et al.*[48] In the experiments, the

Cu_xO foams were used as a working electrode, Au foil as a counter electrode and non-leakage Ag/AgCl (3 M KCl, EDAQ) as a reference electrode. The electrolyte thickness in the X-ray window was adjusted to 1 mm. A Cu foam thickness of 30–40 μm allowed to measure XAS spectra in transmission mode with a sufficient signal-to-noise ratio. As electrolyte, a CO_2-saturated 0.5 M $KHCO_3$ solution (pH = 7.2) was used, which was pumped with a constant flow through the cell using a syringe pump. For the potential increment, step and jump conditions, the following electrochemical experiments were carried out:

(i) Potential increment: $\Delta E = 100$ mV, from + 0.4 V_{RHE} → −1.2 V_{RHE}

(ii) Potential step: OCP → −0.2 V_{RHE} → −0.5 V_{RHE} → −1.3 V_{RHE}

(iii) Potential jump: OCP → −0.5 V_{RHE} or −1.3 V_{RHE}.

3. Results

3.1. *Ex situ* characterization of the annealed Cu_xO foams

The structure, crystallinity, surface and bulk composition of the Cu_xO foams annealed at 100 °C, 200 °C, 300 °C and 450 °C for 12 h in air were investigated using a variety of *ex situ* techniques. Depending on the annealing temperature, the treated Cu_xO foams will be referred to as 100-, 200-, 300-, and 450-foam throughout this work.

Exemplarily, Fig. 1a and b display the SEM images of the Cu_xO foam annealed at 200 °C, showing a two-level foam architecture of interconnected open-cell pores. This hierarchical open pore network structure is prepared by a hydrogen-assisted soft-template electrodeposition process at −3.0 A cm^{-2} for 5 s.[14] The foam thickness is in the range of several tens of μm and is highly porous as determined by Dutta *et al.* using white-light interferometric characterization.[14] The dendritic fine structure is visible in the SEM image at high magnification, see Fig. 1b. The SEM images of the other annealed precursor foams are collected in Fig. S1 in the ESI.† Previous studies have shown that the dendrites undergo structural and compositional alterations during the annealing process.[12] In other words, the thermal annealing in air induces a coalescence of the initial faceted nano-crystallites, resulting in non-textured dendrite structure (Fig. S1a–h†). If the annealing is carried out at 200 °C and above in air, these structural changes are more pronounced and are attributed to the concerted mass transport of oxygen and copper into and out of the dendrites at the Cu_2O/CuO interface formed. The loading and thickness of the Cu_xO foams remain unaffected by the thermal annealing in air.

XRD profiles of all annealed foams are displayed in Fig. 1c. The results of the quantitative Rietveld refinement analysis including the crystal phases, lattice parameters, crystallite sizes and phase quantity are summarized in Table S2.† Obviously, the annealing temperature in an oxidative environment controls the composition of the crystal phases between metallic copper, cuprous oxide (Cu_2O) and cupric oxide (CuO). For the 100- and 200-foams in Fig. 2a, the main crystal phase (≥95 wt%) is

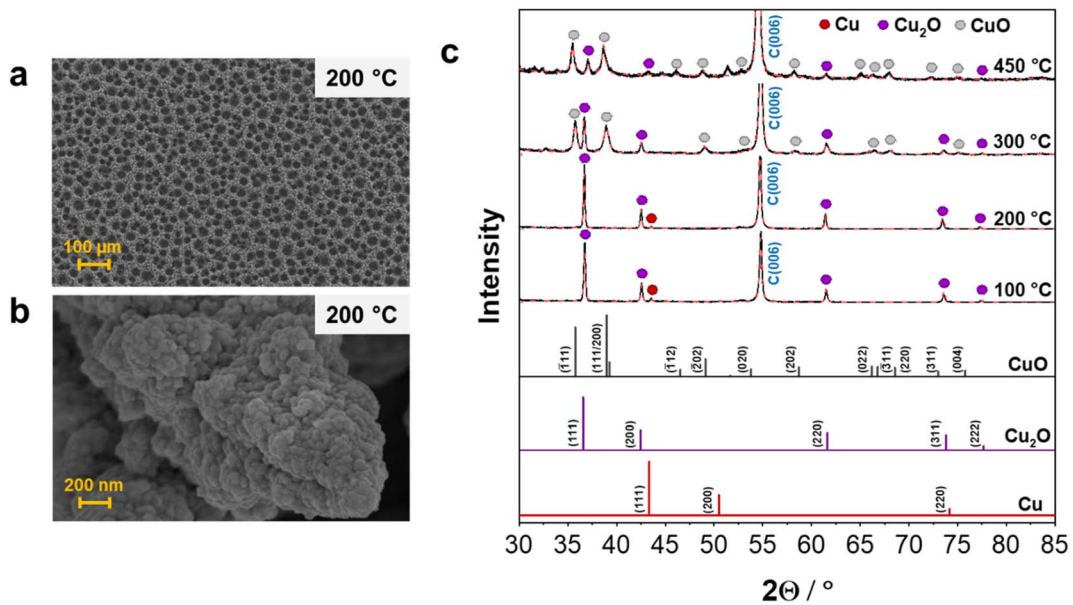

Fig. 1 (a and b) SEM micrographs of the Cu_xO foam annealed at 200 °C for 12 h in air at low and high magnification. (c) XRD profiles (black line) of all annealed Cu_xO foams and the corresponding fits (red dashed line) obtained from the quantitative Rietveld refinement analysis. The references of Cu (#9008468, red), Cu_2O (#1010963, purple) and CuO (#9008961, grey) were taken from the crystal open database (COD).[45–47] Note, that the peak at a 2θ value of 54° labelled C(006) arises from the carbon substrate. For the 100- and 200-foams, the peaks at 2θ values of around 36°, 42°, 61°, 74° and 78° correspond to the lattice planes of (111), (200), (220), (311) and (222) of a primitive cubic Cu_2O unit cell with a space group of $Pn\bar{3}m$. The small peak with 2θ = ~43° is assigned to the lattice plane of (111) for the face-centered cubic (fcc) copper unit cell with a space group of $Fm\bar{3}m$. For the 300- and 450-foams, the additional peaks at 2θ values of ~35°, 39°, 49°, 54°, 59°, 66°, 68° and 76° correspond to the lattice planes of ($\bar{1}11$), (111/200), ($\bar{2}02$), (020) (202), ($\bar{3}11$), (220) and (004) of a base-centered monoclinic unit cell of CuO with space group of $C12/c1$. For the 450-foam, additional CuO peaks appear at 2θ values of ~46°, 65° and 73° that are ascribed to the lattice planes of ($\bar{1}12$), (022) and (311), respectively.

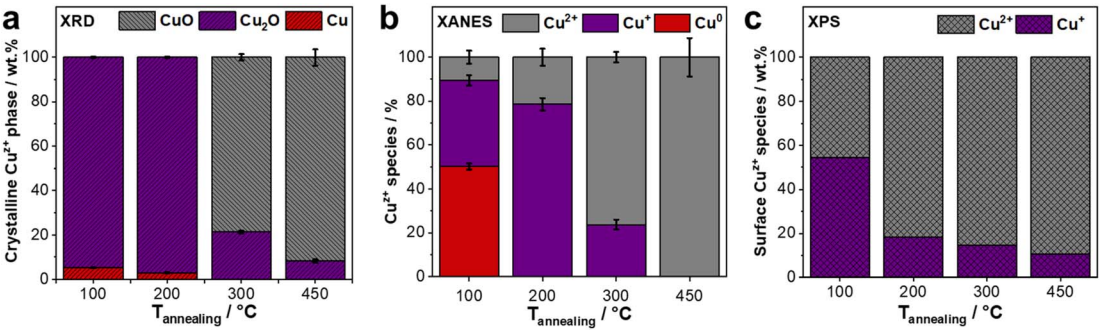

Fig. 2 Contribution of the three copper species (Cu^{2+}, Cu^{+} and Cu^{0}) within the air annealed Cu_xO foams obtained by *ex situ* (a) quantitative Rietveld refinement analysis of the XRD patterns, (b) linear combination fit (LCF) analysis of *ex situ* Cu K-edge XANES spectra and (c) analysis of the high-resolution Cu $2p_{3/2}$ XPS spectra.

cuprous oxide with a space group of $Pn\bar{3}m$. Metallic copper ($Fm\bar{3}m$) appears only as a minor crystalline component. Note that we previously showed that the as-deposited Cu foam already contains sufficient amounts of crystalline Cu_2O phases.[14] In contrast, the annealing temperature of more than 200 °C in air leads to full oxidation of metallic copper and concurrently to the preferred formation of the cupric oxide crystal phase (space group of $C12/c1$). Hence, the 300-foam contains 21 ± 1 wt% Cu_2O and 79 ± 1 wt% CuO, whereas the contribution of the crystalline CuO phase increases to 92 ± 4 wt% upon annealing at 450 °C, see Fig. 2a.

As a complementary bulk technique that can detect the nearest neighboring atoms in the amorphous and crystalline structure, the *ex situ* Cu K-edge XANES data for all foams were evaluated. By measuring the K-edge, the transition of an electron from 1s to 4p orbital occurring on absorption of the X-ray beam is observed, while the sharp increase in the resulting absorption peak is known as the white line. In Fig. S2,† the *ex situ* XANES spectra obtained from the 100-, 200-, 300- and 450-foams and the references of Cu foil, Cu_2O and CuO are plotted. Based on the references, the white line intensity increases from Cu^0 to Cu^{2+} as well as a shift in transition energy occurs from 8979.7 eV (Cu^0), 8981.1 eV (Cu_2O) to 8984.3 eV (CuO), which is in excellent agreement with the literature.[20,49] Additionally, the pre-edge at ~8979 eV in the XANES spectra is distinctive for the Cu^+ and Cu^0 species and is usually much less pronounced for CuO.[49] Fig. 2b shows the contribution of Cu^0, Cu^+ and Cu^{2+} species for the differently annealed Cu_xO foams based on the linear combination fit (LCF) analysis of the *ex situ* XANES data using Cu^0, Cu_2O and CuO reference spectra. The 100-foam consists of 50 ± 1% Cu^0, 39 ± 2% Cu^+ and only 11 ± 3% Cu^{2+} species. The apparent discrepancy between XRD and XANES data can be explained by the amorphous structure of metallic copper within the 100-foam. An annealing temperature of 200 °C leads to an entirely oxidized foam (79 ± 3% Cu^+ and 21 ± 4% Cu^{2+}). Note that due to the sensitivity, the LCF analysis of the XAS data could not detect the minor contribution (3 wt%) of metallic Cu found by XRD. By raising the temperature to 300 °C and 450 °C, the oxidation state of the Cu species within the foam increases further. The 300-foam still contains 24 ± 2% Cu^+ and 76 ± 2% Cu^{2+}, while the foam at 450 °C is entirely oxidized to CuO.

Surface sensitive *ex situ* XPS and Raman spectroscopy were employed to evaluate the initial oxidation states of the Cu_xO foams. High-resolution Cu 2p XPS and Cu LMM Auger spectra for each in air annealed Cu_xO foam are plotted in Fig. S3.† As shown in Fig. S3a,† the deconvolution of Cu $2p_{3/2}$ XPS spectra of the 100-foam indicates two chemical species at binding energies (BEs) of 934.6 eV and 932.0 eV, with the former being assigned to oxidized Cu^{2+} in agreement with other studies.[30,50,51] Additionally, the appearance of the Cu^{2+} satellite peaks between 965 and 960 eV as well as 947 and 938 eV support the presence of CuO surface species.[30,50,51] As shown in Fig. S3b,† a characteristic shift in kinetic energy (KE) to 916.9 eV is detected in the Cu LMM Auger spectrum, which corresponds to Cu_2O.[50,51] Thus, the second chemical species at a BE value of 932.0 eV is assigned to Cu^+. Raising the annealing temperature to 200 °C, the Cu 2p XPS spectrum in Fig. S3c† shows a significant increase of the population of Cu^{2+} surface species, which is also confirmed by the intensity increase of the Cu^{2+} satellites and shift of the Auger KE to 917.1 eV. For the 300- and 450-foams, the Cu LMM Auger spectra (Fig. S3f and h†) and Cu 2p XPS spectra (Fig. S3c and e†) reveal the continuous growth of the population of Cu^{2+} surface species. Based on the deconvolution of the Cu $2p_{3/2}$ XPS spectra, the surface compositions of the differently annealed Cu_xO foams are summarized in Fig. 2c. As expected, metallic Cu on the foam surface is not found at any annealing temperature. Very interestingly, the Cu^+ : Cu^{2+} surface ratio alters from 54 : 46 at 100 °C to 20 : 80 at 200 °C. At 300 °C and 450 °C, the contribution of Cu^{2+} species further increases to 85 wt% and 89 wt%, respectively.

As shown in Fig. S4,† Raman spectra of the different in air annealed Cu_xO foams show Cu_2O and CuO surface species. Note that bulk metallic Cu does not show any Raman active bands due to the polarizability selection rule. In accordance with the XRD data, the 100- and 200-foams show several Raman bands at 110 cm^{-1} (E_μ), 146 cm^{-1} ($T_{1\mu}$), 217 cm^{-1} ($2E_\mu$), 415 cm^{-1} ($4E_\mu$), 623 cm^{-1} ($T_{1\mu}$) and 645 cm^{-1} ($T_{1\mu}$), that are characteristics for crystalline Cu_2O.[52–54] No peaks corresponding to CuO are observed for these two foams. In contrast, the 300- and 450-foams only show characteristic frequencies for the three Raman active modes of CuO at 298 cm^{-1} (A_g), 346 cm^{-1} (B_g) and 632 cm^{-1} (B_g).[52] These findings are consistent with *ex situ* XRD data, as only crystalline copper oxide species exhibit the sharp Raman bands described above.

We can sum up that the *ex situ* XRD and XANES data reveal different bulk contributions of Cu species within the foams particularly annealed at low temperatures. The direct comparison of *ex situ* XRD and XANES data indicates the existence of amorphous CuO species in sufficient amounts at lower annealing temperatures, while the formation of only crystalline Cu_2O phases is signified throughout all annealing temperatures. Furthermore, the surface of the annealed foam is more oxidized compared to the bulk with higher amounts (≥50 wt%) of Cu^{2+} species for the 100- and 200-foams.

To understand the structure–performance–selectivity relationship of the differently annealed Cu_xO foams, the faradaic efficiencies (FEs) and partial current densities for H_2, C1 and C2 product formation at −0.87 V_{RHE} in CO_2-saturated 0.5 M $KHCO_3$ in dependence of the annealing temperature are displayed in Fig. S5.† A notable characteristic of the electrodeposited Cu_xO foam catalysts is the complete suppression of the C1 (methane) reaction pathway.[7] The FEs for CO_2RR products (C1 and C2) are approximately 36%, 39%, 38% and 29% for the 100-, 200-, 300-, and 450-foams, respectively (Fig. S5†). In addition, alcohol formation is observed for all Cu_xO foams after 1 h of the CO_2RR without a clear trend and is therefore not discussed in this work. However, a correlation between C2 products, such as ethylene and ethane and the initial Cu^+ content of the annealed Cu_xO foams (Fig. S6†) could be identified in this work. More precisely, the 100-, 200- and 300-foams show increased FEs (∼9.0–10.0%, ± 0.4%) compared to the 450-foam (∼7.0–8.0%, ± 0.5%), which lacks abundant Cu_2O. This suggests that Cu_2O promotes the formation of C2 products, whereas CuO is less favorable. It is important to note that the FEs for ethylene and ethane in this study are lower than those previously reported by Dutta *et al.*[7] The overall CO_2RR efficiencies were found to be strongly dependent on surface pore size distribution and catalyst film thickness, which are influenced by the deposition time at constant current density. The Cu_xO foams used in this study were optimized for *operando* XAS investigations in terms of film thickness, rather than for CO_2RR product distribution. Consequently, thinner films on a graphite substrate were used here (see Fig. S1,† SEM), which differs from the optimal conditions for high CO_2RR efficiencies. This may have increased the selectivity towards hydrogen as the competing hydrogen evolution reaction (HER) on the partially exposed graphite substrate occurs. The effect is even more pronounced for an annealing temperature of 450 °C, which activates the exposed graphite substrate to produce more hydrogen (Fig. S5†).

In the next step, we investigated the oxide-metal transition during the CO_2RR probed by *operando* Cu K-edge Quick-XAS using different potential control experiments. The different types of experiments conducted (potential increment, step, and jump) are illustrated in Fig. S7.†

3.2. Potential increment experiments ($\Delta E = 100$ mV) from + 0.4 V_{RHE} to −1.2 V_{RHE}

First, potential increment experiments were carried out, where the potential was shifted in steps of 100 mV from + 0.4 V_{RHE} to −1.2 V_{RHE}, while each increment was held for 6–10 min. In order to determine changes in the chemical state of the Cu species, XANES spectra were analyzed using multivariate curve resolution – alternating least squares (MCR-ALS) analysis. A detailed example of the MCR-ALS analysis using MatLab is shown in Fig. S8.† As established by the *ex situ* characterization, the initial chemical states of the Cu_xO foams are mixed oxides irrespective of the annealing temperature. Thus, the reference spectra of the three copper species (Fig. S2†) were fixed as components to obtain the potential-dependent concentration of each Cu species directly from the MCR-ALS algorithm. The series of potential-resolved XANES spectra of the differently annealed Cu_xO foams as well as the corresponding concentration profiles are presented in Fig. 3. Additionally, the Cu K-edge XANES spectra assigned to each potential are displayed in Fig. S9.† Note that there are no changes in the XANES spectra of the different Cu_xO foams at OCP (Fig. S10†). The left panel of Fig. 3 displays the potential-resolved XANES spectra of each annealed Cu_xO foam (100–450 °C). Generally, the series of XANES data show a potential-dependent decrease in white line intensity and shift in transition energy from 8984.3 eV (Cu^{2+}) to 8979.7 eV (Cu^0) for all Cu_xO foams pronounced to different extents. This shift in transition energy indicates a gradual reduction of the Cu^{2+} and Cu^+ species to Cu^0 and is evident to different degrees depending on the annealing temperature.

Based on the LCF analysis of the *ex situ* XANES data (Fig. 2b), the 100-foam initially contains 50% of metallic Cu. Upon exposure to the electrolyte and anodic potentials, this metallic Cu is partially oxidized to Cu^+ species, signified by the increase in the pre-edge and white line intensity observed at +0.4 V_{RHE} and OCP (Fig. S10a†). However, some metallic Cu remains, and consequently, the changes of the pre-edge in the course of the potential-dependent XANES spectra are less pronounced due to this initial content of Cu^0 species. For the Cu^{2+} rich foams annealed at 300 °C and 450 °C (Fig. 3e and g), the potential-resolved XANES spectra recorded at anodic potentials show less pronounced pre-edge features at ∼8979 eV. With increasing cathodic potential, the reduction of Cu_xO is much more evident by the appearance and shift in pre-edge position of the Cu K-edge XANES spectra.

After the potential-induced reduction process to metallic Cu is complete, no further changes in the XANES spectra are found for all annealed Cu_xO foams, signifying that the metallic Cu is stable at more negative potentials than −0.8 V_{RHE}, where typically the formation of hydrocarbon sets in.[12,37] This observation is in excellent agreement with our previous studies.[11,14]

In the right panel of Fig. 3, the normalized concentration of the three Cu species obtained from the MCR-ALS analysis in dependence on the applied potential is displayed for the thermally annealed foams. As the potential is stepwise moved in the cathodic direction, a successive decrease in the Cu^{2+} and Cu^+ species concentrations is observed for all Cu_xO foams. Simultaneously, the concentration of Cu^0 is increasing.

For the 100-foam (Fig. 3b), the exposure to the electrolyte and anodic potential leads to an initial oxidation of 30% Cu^0 to Cu^+ species at + 0.4 V_{RHE}. No change in the concentration (20% Cu^0, 70% Cu^+ and 10% Cu^0 species) occurs until −0.3 V_{RHE}. Thereafter, the successive reduction of Cu^+ and Cu^{2+} species to

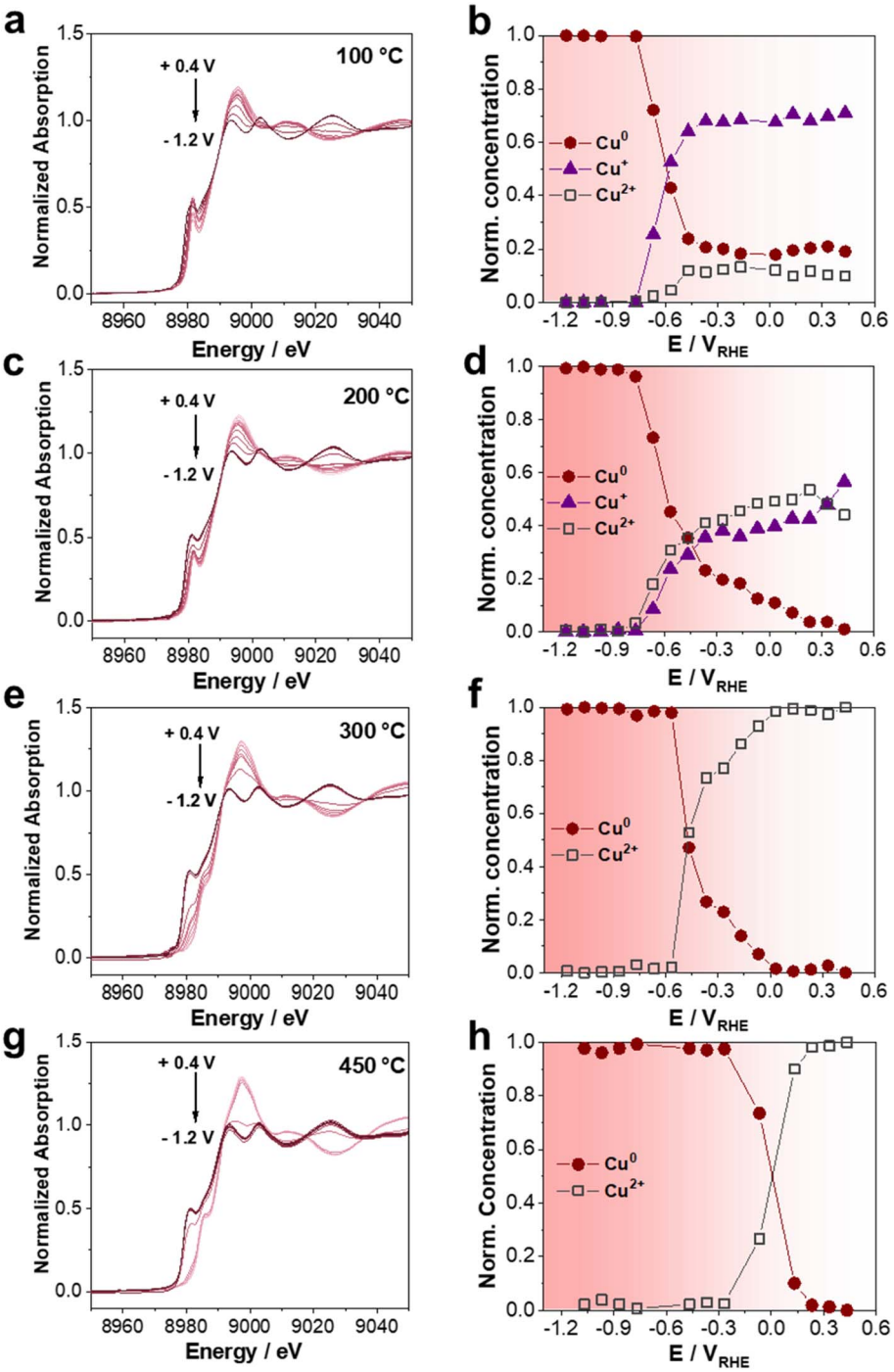

Fig. 3 Left panel (a, c, e and g): series of potential-resolved Cu K-edge XANES spectra of the Cu_xO foams annealed at 100 °C, 200 °C, 300 °C and 450 °C in air. The potential was shifted from +0.4 V_{RHE} to −1.2 V_{RHE} at 100 mV and held for 6–10 min at each potential, while XAS spectra were collected and subsequently averaged. CO_2-saturated 0.5 M $KHCO_3$ was used as electrolyte solution. Right panel (b, d, f and h): normalized Cu^0, Cu^+ and Cu^{2+} concentration courses as a function of the potential obtained by the MCR-ALS analysis of the spectra from the left panel.

metallic Cu sets in and is completed at −0.8 V_{RHE}. For the 200-foam (Fig. 3d), a simultaneous reduction of both Cu^+ and Cu^{2+} species takes place between + 0.2 V_{RHE} and −0.8 V_{RHE}, at which this Cu_xO foam is reduced entirely to metallic Cu. As expected from the *operando* XANES spectra, the initial composition of the 300-foam shows 100% CuO (Fig. 3f), which is gradually reduced to metallic Cu from + 0.4 V_{RHE} to −0.6 V_{RHE}. Here, no formation of Cu^+ species was detected. We note that this observation is different from that in our previously published work, where only 80% of the 300-foam are oxidized to Cu^{2+} species at + 0.5 V_{RHE} with intermediate Cu^+ formation. We attribute this difference to the initial structure, morphology and chemical species of Cu_xO

during the annealing process and in contact with the electrolyte solution.[11,14,30] In contrast, the 450-foam (Fig. 3h), which is also fully oxidized to CuO, shows a completion of the reduction process already at lower anodic potential (−0.3 V_{RHE}), but without the formation of intermediate Cu^+ species. Overall, for all annealed Cu_xO foams the MCR-ALS analysis points out the appearance of metallic Cu at potentials more negative than −0.8 V_{RHE}.

Very interestingly, the transition of oxide to metallic copper occurs at different reduction potentials for each of the different annealing temperatures. We defined the point at which half of this transition was completed as the oxide-metal transition potential.

According to the thermodynamically based Pourbaix diagram, the transition from Cu^{2+} to Cu^+ takes place at + 0.243 V_{SHE} = −0.181 V_{RHE} under the presented conditions (pH = 7.2, CO_2-saturated 0.5 M $KHCO_3$).[55] Only from + 0.045 V_{SHE} = −0.380 V_{RHE} their further electrochemical reduction to Cu^0 sets in.[55] Therefore, the observed differences in the oxide-metal transition potential are very likely based on the initial content of Cu^{2+} species for the differently annealed foams.

Fig. 4 illustrates the changes in oxide-metal transition potential as a function of the annealing temperature and thus the initial concentration of the Cu^{2+} species for all Cu_xO foams obtained from the MCR-ALS analysis. Note that for Cu^+ such a relation is difficult to establish, since the annealing at 100 °C in air already generates high amounts of crystalline Cu_2O. For the 100-foam at a very low Cu^{2+} concentration, the oxide-metal transition potential is found to be at −0.60 V_{RHE}; doubling the annealing temperature to 200 °C and thereby doubling the initial amorphous Cu^{2+} content (surface and bulk obtained from *ex situ* XPS, XAS and XRD) only shifts the oxide-metal transition potential to −0.55 V_{RHE}. A further increase to 300 °C and in Cu^{2+} content to 80% derived from the LCF analysis reduces the potential to −0.45 V_{RHE}, so that at least 50% is in the metallic state. The 450-foam, which contains 100% Cu^{2+} species in the initial state, shows a considerable shift in the oxide-metal transition potential to 0 V_{RHE}.

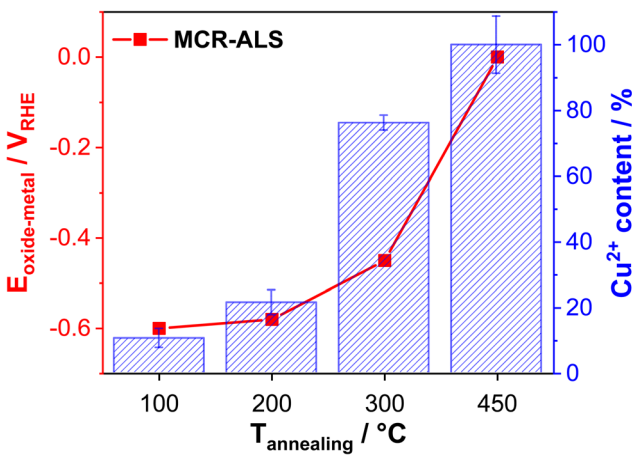

Fig. 4 Oxide-metal transition potential in dependence of the annealing temperature for different Cu_xO foams obtained by MCR-ALS analysis (full red squares). The corresponding Cu^{2+} content of each Cu_xO foam (blue bars) was obtained from LCF analysis of the *ex situ* XANES spectra using Cu^0, Cu_2O and CuO as reference materials.

Additionally, the reduction of the Cu_xO foams can also be monitored by EXAFS analysis. The data are shown in Fig. S11 and Tables S3–S6.† Exemplarily, the EXAFS fit results in *k*- and *R*-space for each of the in air annealed Cu_xO foams at + 0.4 V_{RHE}, −0.1 V_{RHE} and −1.1 V_{RHE} are displayed in Fig. S12–S15.† An increase or decrease in the partial coordination number of the Cu–Cu or Cu–O pair indicates the successive reduction of the Cu_xO foams in the cathodic direction, respectively.

Overall, the oxide-metal transition potential strongly depends on the annealing temperature and therefore the proportion of Cu^{2+} species in the Cu_xO foams. A higher proportion of Cu^{2+} species causes a shift in the oxide-metal transition potential towards lower values during the potential increment experiments (ΔE = 100 mV, from + 0.4 V_{RHE} to −1.2 V_{RHE}) conducted in CO_2-saturated 0.5 M $KHCO_3$.

3.3. Potential step experiments (ΔE >100 mV)

The potential step experiments are the second set of *operando* Quick-XAS measurements carried out to understand the transition of Cu_xO to metallic Cu. The potential was stepwise shifted (more than 100 mV) and held for at least 300 s at each potential (from OCP to −1.3 V_{RHE}) using two intermediate steps at −0.2 V_{RHE} and −0.5 V_{RHE} in CO_2-saturated 0.5 M $KHCO_3$.

In Fig. 5, the respective Cu K-edge Quick-XANES spectra and normalized concentration profiles for the 200-foam from the chronoamperometric measurements at different applied potentials are presented. The series of XANES spectra obtained from the first potential step (OCP to −0.2 V_{RHE} for 700 s) are displayed in Fig. 5a. From thermodynamic predictions, at this potential, the Cu^{2+} species are reduced to Cu^+ at pH = 7.2.[55] As shown in the inset of Fig. 5a, the pre-edge intensity at ~8980 eV increases over time at −0.2 V_{RHE}, indicating the transition from Cu^{2+} to Cu^+. On changing the potential from −0.2 V_{RHE} to −0.5 V_{RHE} (Fig. 5c), a slight decrease in the pre-edge intensity was observed within 350 s, which implies a marginal reduction of Cu^+ to Cu^0. On shifting the potential further to −1.3 V_{RHE}, an instant reduction to Cu^0 takes place within the first 150 s. This is indicated by the white line intensity and shift in transition energy to a lower value as expected for metallic copper.

Furthermore, for the 200-foam, the normalized concentrations of Cu^0, Cu^+ and Cu^{2+} species over time during the chronoamperometric measurements from OCP → −0.2 V_{RHE} → −0.5 V_{RHE} → −1.3 V_{RHE} obtained from the MCR-ALS analysis are displayed in the right column of Fig. 5. As shown in Fig. 5b, at −0.2 V_{RHE} a gradual reduction of the initial 40% Cu^{2+} to Cu^+ is observed and as predicted by thermodynamics, no metallic Cu has started to appear.[55] Around 20% Cu^{2+} remain after 700 s. Jumping to a more cathodic potential of −0.5 V_{RHE} leads to a slow transition of the remaining 10% Cu^{2+} to Cu^+, while after around 100 s the formation of Cu^0 commences. Note that the starting composition at −0.5 V_{RHE} slightly differs from the previous potential jump (at −0.2 V_{RHE}), namely ~10% Cu^{2+} species are reduced. By changing the potential from −0.5 V_{RHE}

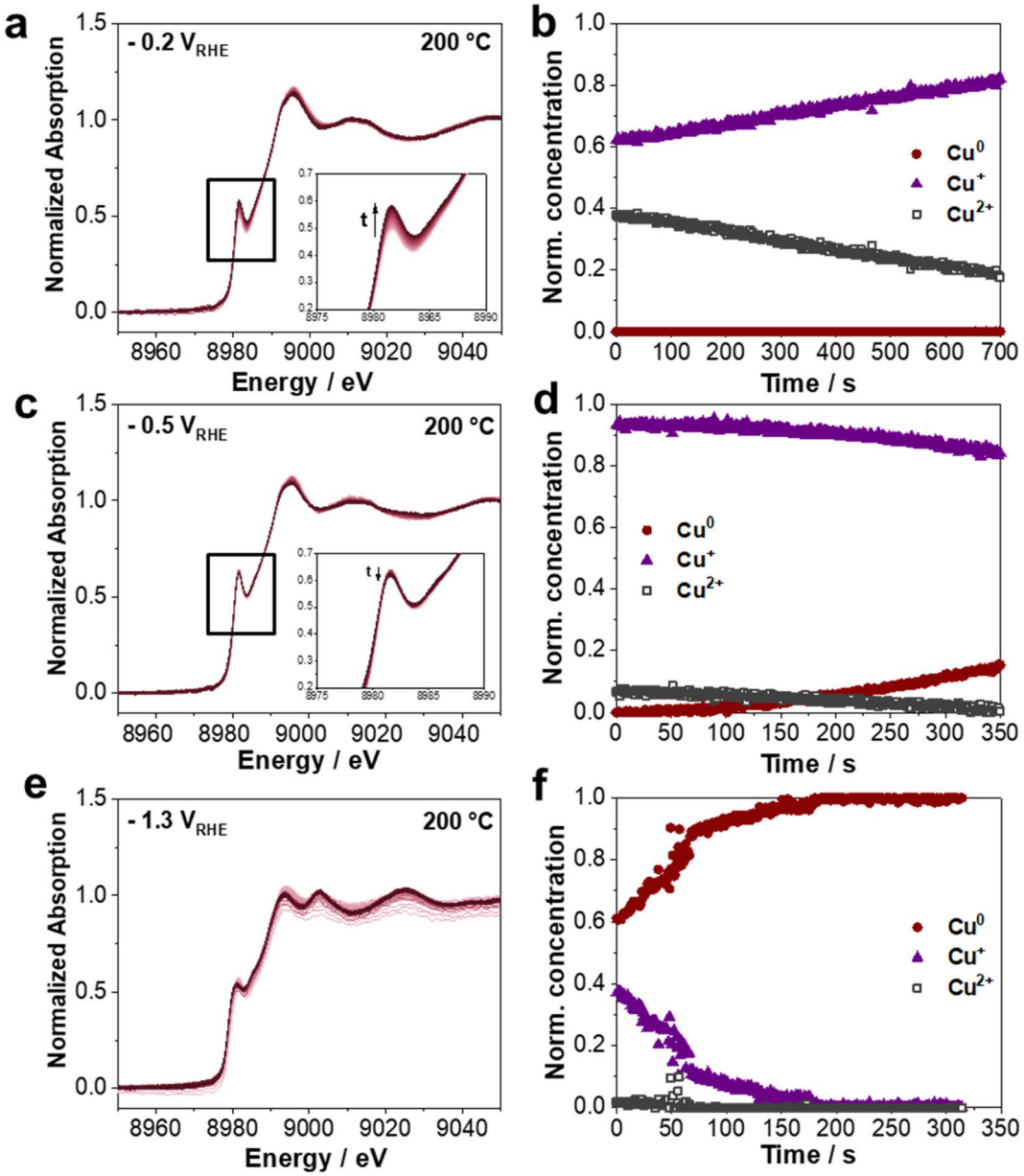

Fig. 5 Series of time-resolved Cu K-edge Quick-XANES spectra of the 200-foam by jumping from OCP → −0.2 V_{RHE} (a) → −0.5 V_{RHE} (c) → −1.3 V_{RHE} (e) in CO_2-saturated 0.5 M $KHCO_3$. One spectrum was collected every second. (b, d and f) Normalized Cu^0, Cu^+ and Cu^{2+} concentrations obtained by the MCR-ALS analysis in dependence of the time at the respective applied potential. Note that the noise in the XAS spectra is caused by the strong bubble formation especially at −1.3 V_{RHE}, making it difficult to normalize the data in a proper way.

to −1.3 V_{RHE} (Fig. 5f), a full reduction of the Cu_xO foam is detected after ~150 s. Thus, the 200-foam with a high Cu^+ content shows a slow transition behavior, which requires highly cathodic potentials to reduce completely from Cu^+ to Cu^0.

The same potential step experiment was carried out for the 450-foam, shown in Fig. S16.† As opposed to the 200-foam, this foam contains 100% of Cu^{2+} species produced by the higher annealing temperature in air. First, only a slight reduction of Cu^{2+} species occurs from OCP to −0.2 V_{RHE}. About 10% of the Cu^{2+} species are reduced to Cu^0 and Cu^+ species within 350 s. However, on changing the potential from −0.2 V_{RHE} to −0.5 V_{RHE}, an instant reduction of Cu^{2+} and Cu^+ species within less than 2 s is detected. Thus, the higher content of Cu^{2+} species in the 450-foam leads to a shift in the potential-induced oxide-metal transition to less negative potentials and is much faster compared to the reduction behavior of the 200-foam.

Altogether, for the 200-foam, an initial reduction of Cu^{2+} to Cu^+ at −0.2 V_{RHE} and a slow transition of the Cu^+ to metallic at −0.5 V_{RHE} are observed. In contrast, the 450-foam already rapidly reduces to metallic Cu at −0.5 V_{RHE}.

3.4. Potential jump experiments ($\Delta E \geq 500$ mV)

In order to investigate the oxide-metal transition behavior without applying intermediate potentials, a direct potential

jump from OCP to either −0.5 V_{RHE} or −1.3 V_{RHE} in CO_2-saturated 0.5 M $KHCO_3$ was performed.

In Fig. 6, the direct potential jump from OCP to −0.5 V_{RHE} is plotted for the 200- and 300-foams, whereas the larger jump to −1.3 V_{RHE} for the 100- and 300-foams is displayed in Fig. 7. Both Fig. 6 and 7 illustrate a series of time-resolved Cu K-edge QuickXANES spectra collected at the applied potentials with the corresponding normalized concentration profiles and holding times obtained by the MCR-ALS analysis. Again, the composition of each Cu species obtained by the MCR-ALS analysis is determined using the CuO, Cu_2O and metallic Cu references.

Fig. 6a illustrates the time-resolved changes in the QuickXANES data for the 200-foam by jumping the potential from OCP to −0.5 V_{RHE} for ∼300 s. A slow decrease in white line intensity and a shift in edge jump energy from 8982.1 eV (Cu^{z+}) to 8979.7 eV (Cu^0) are observed. Furthermore, the inset of Fig. 6a shows a decrease in the pre-edge intensity within 300 s at −0.5 V_{RHE}. Based on the MCR-ALS analysis, initially, 63% Cu^+ and 37% Cu^{2+} species are present by directly applying a potential of −0.5 V_{RHE}. This is in good agreement with the initial compositions obtained during the potential increment and step experiments for this Cu_xO foam. First, we observed that the Cu^{2+} species diminishes from 37% to 0% at −0.5 V_{RHE} for around 225 s (Fig. 6b). Within a holding time of 130 s, a simultaneous increase in Cu^+ species as the intermediate is found at a similar rate, at which the initial Cu^{2+} species decreases. From 130 s onwards, the formation of metallic Cu commences and is complete after 285 s at −0.5 V_{RHE}. As a comparison, the Cu^+ intermediate species were already observed for the 200-foam during the potential step experiment as shown in Fig. 5. Therefore, we can conclude that the electrochemical reduction of the Cu^{2+} to Cu^+ took place initially, followed by the formation of fully metallic Cu under these conditions.

The same potential jump experiment (OCP → −0.5 V_{RHE}) was carried out with the 300-foam. A series of Cu K-edge QuickXANES spectra collected for 130 s at −0.5 V_{RHE} (presented in Fig. 6c) show a fast decrease in white line intensity and a small shift in transition energy from 8981.5 eV (Cu^{z+}) to 8980.0 eV (Cu^0). This quick potential-induced oxide-metal transition is clearly confirmed by the MCR-ALS analysis (Fig. 6d). A prompt reduction of the initial Cu_xO to metallic within ∼40 s is observed based on the decrease in Cu^+ and Cu^{2+} species and concurrent increase in the Cu^0 concentration. It is noted that half of the Cu^{2+} and Cu^+ content was already reduced after around 20 s by jumping the potential from OCP to −0.5 V_{RHE}. Thus, it is obvious that the oxide to metal transition processes for the 200- and 300-foams from OCP to −0.5 V_{RHE} occur with different kinetics depending on the initial chemical state of the

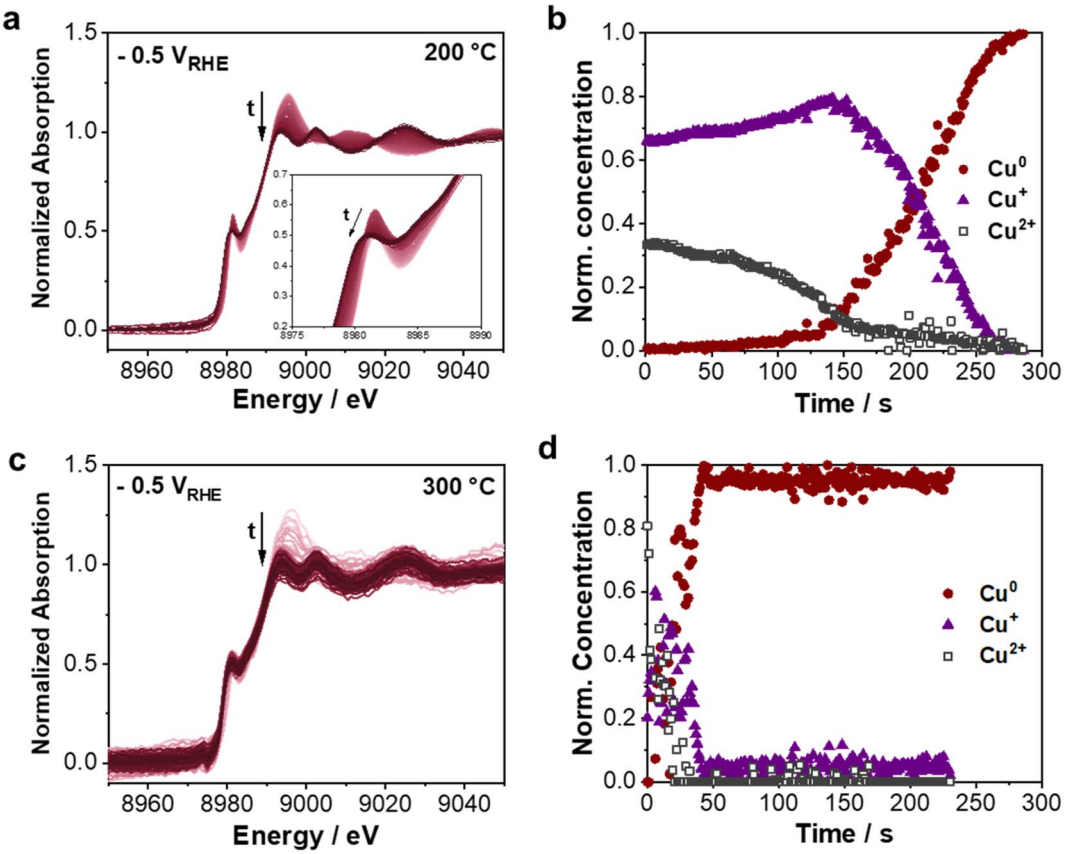

Fig. 6 Time-resolved changes in Cu K-edge XANES spectra of the 200-foam (a and b) and 300-foam (c and d) by direct switching of the potential from OCP → −0.5 V_{RHE}. One spectrum was collected every second. (b and d) Normalized concentration profiles of the Cu^{2+}, Cu^+ and Cu^0 species obtained by the MCR-ALS analysis. All measurements were performed in CO_2-saturated 0.5 M $KHCO_3$. Note that the noise in the XAS spectra is caused by the strong bubble formation especially at −0.5 V_{RHE}, making it difficult to normalize the data in a proper way.

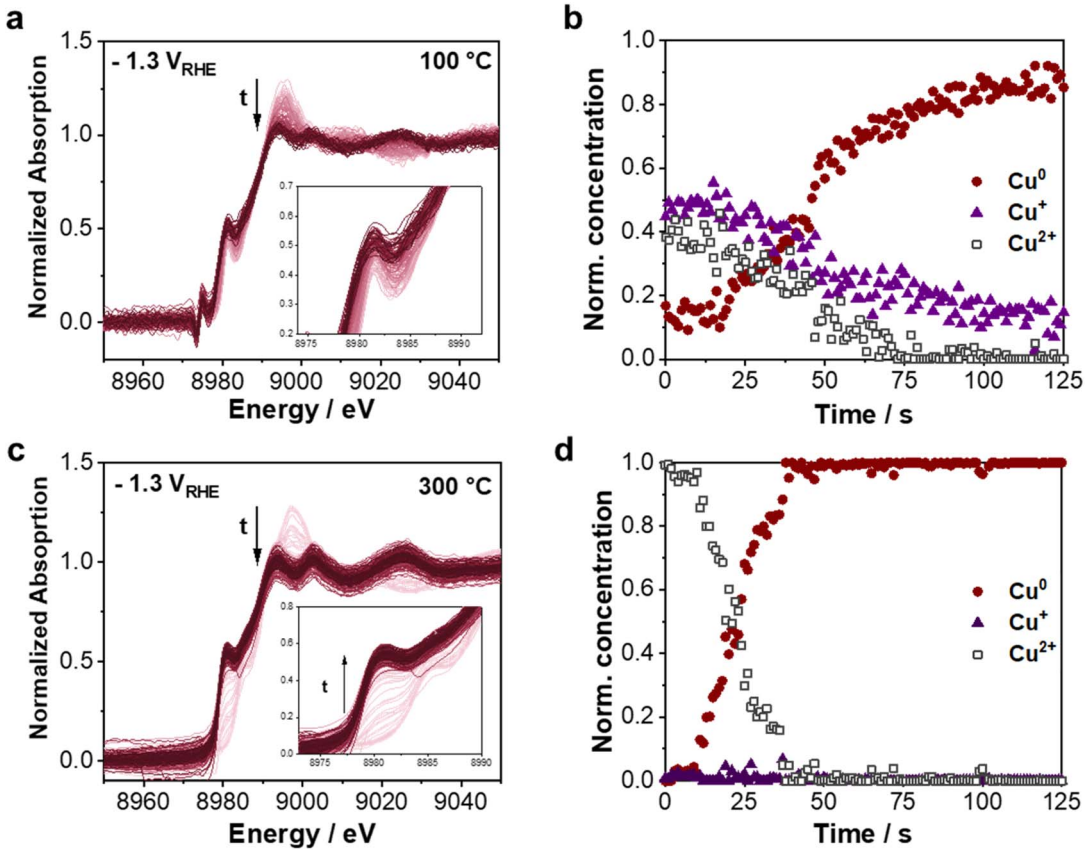

Fig. 7 Series of time-resolved Cu K-edge Quick-XANES spectra of 100-foam (a and b) and 300-foam (c and d) by direct jumping of the potential from OCP → −1.3 V_{RHE}. One spectrum was collected every second. (b and d) Normalized concentration profiles of the Cu^{2+}, Cu^{+} and Cu^{0} species obtained by the MCR-ALS analysis. All measurements were performed in CO_2-saturated 0.5 M $KHCO_3$. Note that the noise in the XAS spectra is caused by the strong bubble formation especially at −1.3 V_{RHE}. This makes it difficult to normalize the data in a proper way.

copper. More precisely, the oxide-metal transition kinetics of the 200-foam with an initial Cu^{+} : Cu^{2+} ratio of 63 : 37 is around 6-times slower than that for the 300-foam (Cu^{+} : Cu^{2+} ratio of 20 : 80).

The transition behavior of the 100-foam from OCP to −1.3 V_{RHE} is shown in Fig. 7a and b. From the course of the time-resolved Quick-XANES spectra (Fig. 7a), a decrease in the white line intensity, but only minimal changes in the pre-edge are observed within a holding time of 125 s at −1.3 V_{RHE}. Again, for the 100-foam, this trend can be explained by the high initial Cu^{0} content (~20% at −1.3 V_{RHE} within the first seconds). Evidently, the time-dependent changes in the spectra are less pronounced compared to the entirely oxidized foams, *e.g.* 300- and 450-foams. From the MCR-ALS analysis (Fig. 7b), for the 100-foam, the reduction to metallic Cu is not fully completed within 125 s at −1.3 V_{RHE} (~10% Cu^{+} remain), while half the Cu_xO is already transformed into the metallic state after ~50 s. Interestingly, as a potential of −1.3 V_{RHE} (starting from OCP) was applied instead of −0.5 V_{RHE} (Fig. 7c and d), the oxide-metal transition process for the 300-foam is not getting faster. At −1.3 V_{RHE} the reduction to metallic Cu species also took place within ~40 s, while the Cu^{2+} concentration dropped to 0% during this time. Similarly, the time at which half of the Cu^{z+} content is reduced to Cu^{0} was the same (around 25 s). Note that, compared to the potential jump to −0.5 V_{RHE}, no Cu^{+} species are observed for the 300-foam. As shown in Fig. 7c, the time-dependent XANES spectra clearly support the oxide-metal reduction by the shift and decrease in white line intensity for the 300-foam. Furthermore, the characteristic increase in pre-edge and shift in transition energy from ~8985 eV (mainly Cu^{2+}) to ~8980 eV (Cu^{0}) corroborate the findings from the MCR-ALS.

As the potential jump experiments revealed a 6-times slower oxide-metal reduction of the Cu^{+} rich 200-foam compared to the Cu^{2+} rich 300-foam at the same potential (−0.5 V_{RHE}), we can conclude that the abundance of Cu^{2+} species strongly influences the oxide-metal transition kinetics. More precisely, from *ex situ* XANES and XPS analyses for the 100- and 200-foams, lower amounts of the Cu^{2+} species (~20–40%) are incorporated in the amorphous oxide mainly located at the surface, while the XRD data do not indicate the formation of crystalline CuO phases. Based on the XRD data, only crystalline Cu_2O phases are present throughout these foams, while the 300-foam consists of ~76 wt% crystalline CuO.

4. Discussion

Fig. 8 and 9 summarize the principal findings of this study, showing schematically the different reduction rates and life-times of Cu^{2+}, Cu^{+} and Cu^{0} species in dependence of the applied

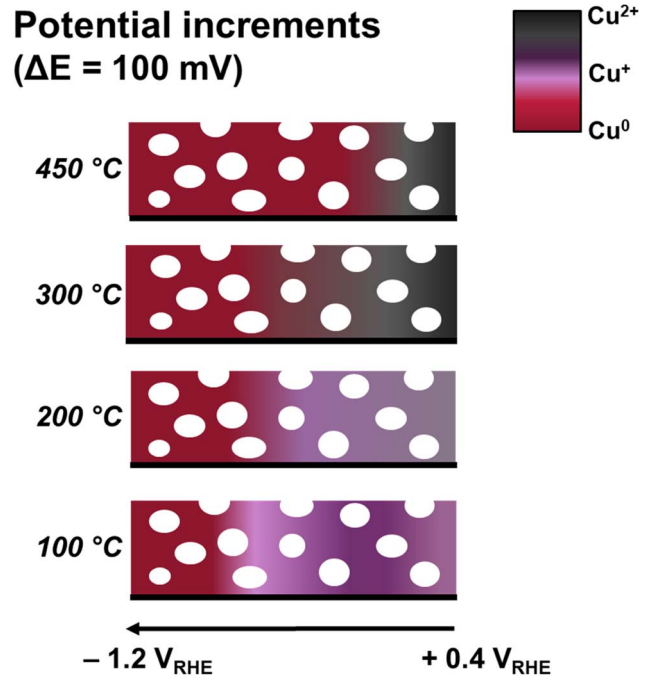

Fig. 8 Schematic model showing the potential-dependent oxide-metal transition processes of the four differently annealed Cu_xO foams during the potential increment (ΔE = 100 mV) experiments. The transition of Cu^{2+} to Cu^0 with intermediate Cu^+ formation is illustrated. From the *ex situ* XANES analysis, the initial $Cu^0 : Cu^+ : Cu^{2+}$ ratios of the in air annealed Cu_xO foams are 50 : 39 : 11 (100 °C), 0 : 79 : 21 (200 °C), 0 : 24 : 76% (300 °C) and 0 : 0 : 100 (450 °C), respectively. The pore structure of the foams is depicted by the white spheres.

potential for the Cu_xO foams annealed at 100 °C, 200 °C, 300 °C and 450 °C for 12 h in air. Especially in this work, the differences observed between small potential increments *vs.* (large) potential steps/jumps are highlighted as well as the shift of the oxide-metal transition potential with the annealing temperature and thus the initial ratios of $Cu^0 : Cu^+ : Cu^{2+}$ species and structure of these Cu_xO foams.

First, our results demonstrated that the annealing temperature has a strong influence on the $Cu^0 : Cu^+ : Cu^{2+}$ ratio within the bulk and surface of the Cu_xO foams as well as the crystal structure of the CuO species. Generally, the content of Cu^{2+} species and their degree of crystallinity increase with higher annealing temperature, while crystalline Cu_2O is present throughout all annealed Cu_xO foams. The results from the *ex situ* XRD and Raman data show a high crystallinity of the CuO phase after annealing at and above 300 °C, while at lower temperatures the CuO detected by the XANES and XPS techniques is strongly amorphous (absence of peaks in the XRD profile). Secondly, the annealing at lower temperatures leads to strong differences in the surface and bulk composition of the treated foams. Consequently, more amorphous CuO species on the foam surface are present at lower annealing temperatures. As an excellent example, the 200-foam contains ~80 wt% (*via* XPS) of amorphous CuO surface species, while the bulk-like XANES data only shows 20% CuO. These differences in the oxidation state, crystallinity and bulk *vs.* surface Cu oxide as well as the applied electrochemical protocol have a strong influence on the oxide to metal reduction processes during the CO_2RR, which will be discussed now.

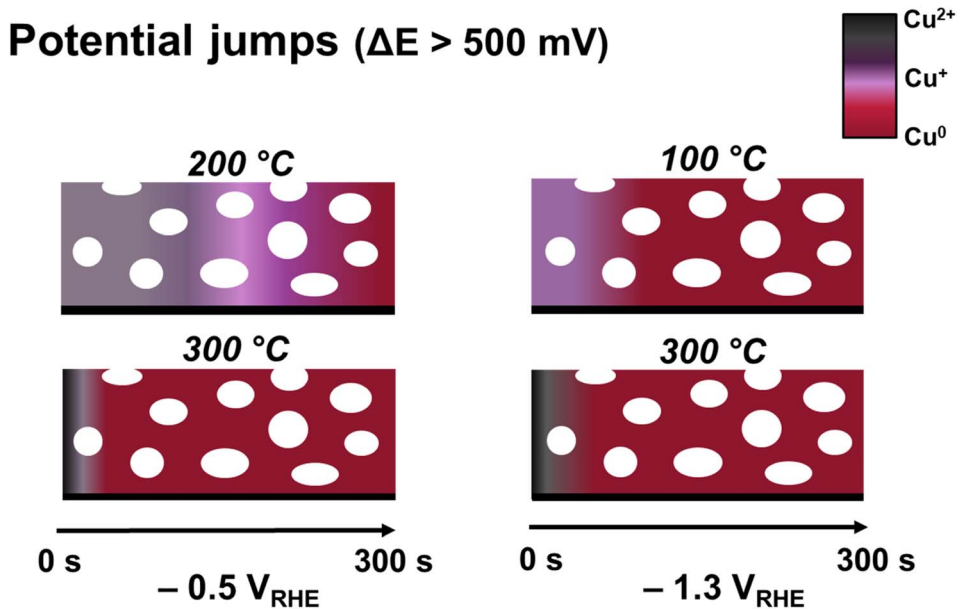

Fig. 9 Schematic model showing the time-dependent oxide-metal transition processes of the 100 °C, 200 °C and 300 °C in air annealed Cu_xO foams during the potential jump (ΔE > 500 mV) experiments. The fast transition of Cu^{2+} to Cu^0 *vs.* slower intermediate Cu^+ formation is illustrated for the two different chronoamperometric experiments used in this study. From the *ex situ* XANES analysis, the initial $Cu^0 : Cu^+ : Cu^{2+}$ ratios of the in air annealed Cu_xO foams are 50 : 39 : 11 (100 °C), 0 : 79 : 21 (200 °C), 0 : 24 : 76 (300 °C) and 0 : 0 : 100 (450 °C), respectively. The pore structure of the foams is depicted by the white spheres.

The potential increment conditions (ΔE = 100 mV, from +0.4 V_{RHE} to −1.2 V_{RHE} for 6–10 min at each potential) give insights into the stepwise oxide-metal transition processes of the Cu_xO foams (Fig. 8). From these experiments, we demonstrated that the higher the annealing temperature of the precursor foam and thus the higher the concentration of crystalline CuO species, the lower the oxide-metal transition potential. Thus, the 100-foam shows the highest cathodic oxide-metal transition potential, whereas the lowest overpotential is required for the 450-foam. The difference in the transition potential between the 100- and 450-foams is therefore around −600 mV. Consequently, highly crystalline CuO phases can be electrochemically reduced at much lower potentials compared to amorphous CuO.

Considering that the oxide-metal transition affects the CO_2RR product distribution and faradaic efficiencies, it is important to understand the kinetics of this process for the design of efficient electrocatalysts. In all experiments, a chronoamperometry method is applied showing an exponential current decay over time at constant potential due to the transition from the faradaic current to mass-transport limiting current. According to the thermodynamically predicted Pourbaix diagram, the reduction pathway of Cu^{2+} species to metallic always involves the formation of Cu^+ intermediate species under these CO_2RR conditions (pH = 7.2, 25 °C).[55] In the first obvious assumption, the electrochemical oxide-metal transition dynamics might comprise two rate constants. One for the reduction rate from Cu^{2+} to Cu^+ (k_1) and one from Cu^+ to Cu^0 (k_2). Depending on which one of the potential-controlled rate constants is the rate determining step (rds), *i.e.* the slowest step, it allows detection of Cu^+ formation or it might be too fast to be observed with the technique used in this study (resolution of 1 s for each XANES spectrum). If k_1 is rate determining, the Cu^+ intermediate rapidly reacts to Cu^0 species, which cannot be probed within the one second of data acquisition. On the other hand, if k_2 is the slowest step, a fast buildup of Cu^+ occurs followed by a slow reduction step to metallic Cu. In this work, we can only evaluate the relative relation between k_1 and k_2 with each other.

With the potential step (OCP → −0.2 V_{RHE} → −0.5 V_{RHE} → −1.3 V_{RHE}) and potential jump (OCP → −0.5 V_{RHE} or −1.3 V_{RHE}) experiments, we gained an understanding of the kinetics during this transition process and the respective lifetime of each Cu^{z+} species without applying intermediate potentials in between. We could demonstrate that for the 200-foam first one-electron-transfer from Cu^{2+} to Cu^+ sets in, while applying intermediate potentials at −0.2 V_{RHE} and −0.5 V_{RHE}. Once the oxide-metal transition potential was reached, further reduction to metallic Cu occurred almost instantly. Again, we found that with increasing annealing temperature, *i.e.* for the 450-foam compared to the 200-foam, the reduction potential to Cu^0 is shifted to less negative values. We suggest that the observed differences in the kinetics are controlled by the abundance of crystalline CuO species.

With the potential jump conditions (from OCP to −0.5 V_{RHE} or −1.3 V_{RHE}), we were able to show the initial Cu^+ formation/reduction only for the 200- and 100-foams (Fig. 9). However, for the 300-foam, the reduction rate to Cu^+ species is fast, but can only be detected at the start of the measurement at −0.5 V_{RHE}. For this annealing temperature, the reduction of Cu^{2+} and Cu^+ species to metallic Cu was already completed within ∼40 s, which is 6-times faster compared to the 200-foam using the same protocol (from OCP to −0.5 V_{RHE}). At −1.3 V_{RHE} the Cu^+ formation is too fast to be detected within 1 s of the XAS acquisition. Our observation can be explained by the different reduction rates and lifetimes of Cu^{2+}, Cu^+ and Cu^0 species during the electrochemical reduction processes. Based on the complementary *ex situ* techniques, the 300-foam mainly consists of crystalline CuO, while for the 200-foam, the Cu^{2+} species are incorporated in the amorphous oxide and mainly located at the surface.

On comparing the potential step (ΔE >100 mV) and jump experiments (ΔE >500 mV) for the 200-foam, different oxide to metal reduction behaviors were found (Fig. 9). For the 200-foam, jumping directly from OCP to −0.5 V_{RHE} (Fig. 6a) without any intermediate potential steps shows an initial Cu^{2+} to Cu^+ transition. Therefore, the rds is the Cu^+ to Cu^0 reduction, implying a small k_2. Additionally, the metallic Cu formation only sets in after ∼130 s, resulting in a buildup of Cu^+ species by holding the potential at −0.5 V_{RHE}. For the 200-foam, the complete reduction to metallic Cu is reached after ∼285 s in this experiment. In contrast, under the potential step conditions, where −0.2 V_{RHE} was applied before −0.5 V_{RHE}, only around 20% Cu^0 were formed at −0.5 V_{RHE} after the same time. Thus, without intermediate potential steps a faster reduction to metallic copper at −0.5 V_{RHE} occurs, pointing out the strong impact of the previously applied potential to the reduction behavior of Cu^+.

Furthermore, for the 300-foam, the reduction process becomes much faster if no intermediate potential steps were conducted beforehand. More precisely, the jump from OCP directly to the oxide-metal transition potential of ∼ −0.5 V_{RHE} leads to an instant reduction within 40 s. This is contrary to the observation, where increment potential steps were applied. Here, the reduction to metallic Cu is only complete at −0.6 V_{RHE}. We note that there is a discrepancy between our previously published XAS analysis of the 300-foam, where a clear intermediate formation of Cu^+ species occurs during the potential step experiments before the reduction to metallic Cu commences.[14] However, initially at +0.4 V_{RHE}, our analysis clearly indicates that this Cu_xO foam is fully oxidized to Cu^{2+} species, while previously around 20% remained as Cu^+ species even at applied anodic potentials.[14] We explain this observation by the initial structure and chemical species of Cu_xO during the annealing process and in contact with the electrolyte solution. Based on the potential step (ΔE >100 mV) and jump experiments (ΔE >500 mV), we suggest that the sluggish reduction kinetics for the 100- and 200-foams are correlated with the surface concentration of amorphous CuO as well as the high abundance of Cu^+ species, which is favorable for the formation of C2 products during the CO_2RR. Only the crystalline CuO phase found for the 300- and 450-foams undergoes very fast reduction kinetics at lower cathodic potentials applied.

Altogether, we reveal a clear dependence of the Cu^0 : Cu^+ : Cu^{2+} ratio, crystal structure and electrochemical protocol applied on the oxide-metal reduction kinetics for the differently annealed Cu_xO foams. A high concentration of Cu^{2+} species as well-ordered CuO

phase is able to influence the rds of the oxide-metal transition, resulting in a shift to lower cathodic potentials and therefore a lower energy barrier to reduction. Comparing the different chronoamperometric protocols, we show that during the smaller potential step and increment experiments, a slowdown of the reduction of the Cu^{2+}/Cu^{+} to Cu^{0} occurs. Thus, jumping directly to a highly cathodic potential enhances the reduction kinetics of Cu_xO to metallic Cu.

Our *operando* Quick-XAS study provides deeper insights into the oxide-metal transition dynamics of Cu_xO-derived electrocatalysts and uncovers the impact of the electrochemical protocol on the reduction of the Cu oxide to metallic species as well as the presence of amorphous/crystalline CuO phases during CO_2 electrolysis.

5. Conclusion

In this work, we investigated the potential and time dependent oxide-metal transition dynamics for the Cu_xO foams annealed in air at four different temperatures ranging from 100 °C to 450 °C probed by *operando* Quick-XAS. From the comparison of *ex situ* XANES, XRD and XPS analyses, we pointed out that an increase in annealing temperature leads to an increase in the proportion of Cu^{2+} species and their degree of crystallinity within the Cu_xO foams. More precisely, after annealing at 100 °C and 200 °C these CuO species are amorphous and mainly found at the surface of the foam. Once the annealing temperature reaches 300 °C or higher, the CuO phase is entirely crystalline.

Using potential increment ($\Delta E = 100$ mV), step ($\Delta E >100$ mV) and jump ($\Delta E \geq 500$ mV) experiments, we gained deeper insights into the transition kinetics from $Cu^{2+} \rightarrow Cu^{+} \rightarrow Cu^{0}$ in CO_2-saturated 0.5 M $KHCO_3$. These different types of potential control experiments strongly influence the reduction behavior of Cu_xO to metallic Cu under cathodic conditions. In other words, using smaller increments slows down the reduction kinetics. Additionally, from the potential increment experiments, an increase in initial crystalline CuO species leads to a shift in the oxide-metal transition towards less negative potentials, signifying a lower energy barrier to reduction.

A change in the rate determining step during the reduction pathway with the stability of Cu_2O intermediates was identified. For the crystalline CuO rich foams (300 °C and 450 °C), a large rate constant k_2 at highly cathodic potentials results in a very fast transition from Cu^{+} to Cu^{0}. For all in air annealed Cu_xO foams, we showed that the catalytically active species in the potential range of hydrocarbon formation,[10] at -0.8 V_{RHE} and more negative potentials, is entirely metallic Cu.

Overall, the *operando* Quick-XAS study reveals a clear dependence of the $Cu^{0}:Cu^{+}:Cu^{2+}$ ratio and structure of the CuO species as well as a strong influence of the applied potential protocol on the oxide-metal reduction kinetics for the differently annealed Cu_xO foams.

Data availability

The data supporting this article have been included as part of the ESI.†

Conflicts of interest

There are no conflicts to declare.

Acknowledgements

The Swiss Light Source (SLS) at the Paul Scherrer Institute, Switzerland, is thanked, in particular Dr Adam Clark and Dr Maarten Nachtegaal for access to synchrotron beamline SuperXAS (proposal-IDs 20161388 and 20182014). Specifically, we would like to acknowledge the advice on XAS data analysis using MCR-ALS by Dr Valérie Briois and Dr Stéphanie Belin from the ROCK Beamline at Soleil Synchrotron, France. We thank the DFG for funding the ESCALAB 250 Xi XPS spectrometer (INST 184/144-1 FUGG) and WITec alpha300 RSA confocal microscope (INST 188/517-1 FUGG).

References

1 T. Haas, R. Krause, R. Weber, M. Demler and G. Schmid, Technical photosynthesis involving CO2 electrolysis and fermentation, *Nat. Catal.*, 2018, **1**, 32–39.
2 J. W. Vickers, D. Alfonso and D. R. Kauffman, Electrochemical Carbon Dioxide Reduction at Nanostructured Gold, Copper, and Alloy Materials, *Energy Technol.*, 2017, **5**, 775–795.
3 S. Bhardwaj, A. Biswas, M. Das and R. S. Dey, Nanostructured Cu foam and its derivatives: emerging materials for the heterogeneous conversion of CO 2 to fuels, *Sustainable Energy Fuels*, 2021, **5**, 2393–2414.
4 S. Nitopi, E. Bertheussen, S. B. Scott, X. Liu, A. K. Engstfeld, S. Horch, B. Seger, I. E. L. Stephens, K. Chan, C. Hahn, J. K. Nørskov, T. F. Jaramillo and I. Chorkendorff, Progress and Perspectives of Electrochemical CO2 Reduction on Copper in Aqueous Electrolyte, *Chem. Rev.*, 2019, **119**, 7610–7672.
5 A. Rendón-Calle, S. Builes and F. Calle-Vallejo, A brief review of the computational modeling of CO2 electroreduction on Cu electrodes, *Curr. Opin. Electrochem.*, 2018, **9**, 158–165.
6 *Modern Aspects of Electrochemistry*, ed. Y. Hori, C. G. Vayenas, R. E. White and M. E. Gamboa-Aldeco, 2008, vol. 42, pp. 89–189.
7 A. Dutta, M. Rahaman, N. C. Luedi, M. Mohos and P. Broekmann, Morphology Matters: Tuning the Product Distribution of CO 2 Electroreduction on Oxide-Derived Cu Foam Catalysts, *ACS Catal.*, 2016, **6**, 3804–3814.
8 B. Hecker, C. Dosche and M. Oezaslan, Ligament Evolution in Nanoporous Cu Films Prepared by Dealloying, *J. Phys. Chem. C*, 2018, **122**, 26378–26384.
9 S. Ibrahim, A. Dworzak, D. Crespo, F. U. Renner, C. Dosche and M. Oezaslan, Nanoporous Copper Ribbons Prepared by Chemical Dealloying of a Melt-Spun ZnCu Alloy, *J. Phys. Chem. C*, 2022, **126**, 212–226.
10 M. Rahaman, A. Dutta, A. Zanetti and P. Broekmann, Electrochemical Reduction of CO 2 into Multicarbon Alcohols on Activated Cu Mesh Catalysts: An Identical Location (IL) Study, *ACS Catal.*, 2017, **7**, 7946–7956.

11 A. Dutta, K. Kiran, M. Rahaman, I. Z. Montiel, P. Moreno-García, S. Vesztergom, J. Drnec, M. Oezaslan and P. Broekmann, Insights from Operando and Identical Location (IL) Techniques on the Activation of Electrocatalysts for the Conversion of CO_2: A Mini-Review, *Chimia*, 2021, **75**, 733–743.

12 M. Le, M. Ren, Z. Zhang, P. T. Sprunger, R. L. Kurtz and J. C. Flake, Electrochemical Reduction of CO2 to CH3OH at Copper Oxide Surfaces, *J. Electrochem. Soc.*, 2011, **158**, E45.

13 R. Daiyan, W. H. Saputera, Q. Zhang, E. Lovell, S. Lim, Y. H. Ng, X. Lu and R. Amal, 3D Heterostructured Copper Electrode for Conversion of Carbon Dioxide to Alcohols at Low Overpotentials, *Adv. Sustainable Syst.*, 2019, **3**, 1800064.

14 A. Dutta, M. Rahaman, B. Hecker, J. Drnec, K. Kiran, I. Zelocualtecatl Montiel, D. Jochen Weber, A. Zanetti, A. Cedeño López, I. Martens, P. Broekmann and M. Oezaslan, CO2 electrolysis – Complementary operando XRD, XAS and Raman spectroscopy study on the stability of CuxO foam catalysts, *J. Catal.*, 2020, **389**, 592–603.

15 W. Tang, A. A. Peterson, A. S. Varela, Z. P. Jovanov, L. Bech, W. J. Durand, S. Dahl, J. K. Nørskov and I. Chorkendorff, The importance of surface morphology in controlling the selectivity of polycrystalline copper for CO2 electroreduction, *Phys. Chem. Chem. Phys.*, 2012, **14**, 76–81.

16 K. W. Frese, Electrochemical Reduction of CO 2 at Intentionally Oxidized Copper Electrodes, *J. Electrochem. Soc.*, 1991, **138**, 3338–3344.

17 R. Kas, R. Kortlever, A. Milbrat, M. T. M. Koper, G. Mul and J. Baltrusaitis, Electrochemical CO2 reduction on Cu2O-derived copper nanoparticles: controlling the catalytic selectivity of hydrocarbons, *Phys. Chem. Chem. Phys.*, 2014, **16**, 12194–12201.

18 C. W. Li, J. Ciston and M. W. Kanan, Electroreduction of carbon monoxide to liquid fuel on oxide-derived nanocrystalline copper, *Nature*, 2014, **508**, 504–507.

19 D. Gao, I. Zegkinoglou, N. J. Divins, F. Scholten, I. Sinev, P. Grosse and B. Roldan Cuenya, Plasma-Activated Copper Nanocube Catalysts for Efficient Carbon Dioxide Electroreduction to Hydrocarbons and Alcohols, *ACS Nano*, 2017, **11**, 4825–4831.

20 H. Mistry, A. S. Varela, C. S. Bonifacio, I. Zegkinoglou, I. Sinev, Y.-W. Choi, K. Kisslinger, E. A. Stach, J. C. Yang, P. Strasser and B. R. Cuenya, Highly selective plasma-activated copper catalysts for carbon dioxide reduction to ethylene, *Nat. Commun.*, 2016, **7**, 12123.

21 B. Beverskog and I. Puigdomenech, Revised Pourbaix Diagrams for Copper at 25 to 300°C, *J. Electrochem. Soc.*, 1997, **144**, 3476–3483.

22 F. Cavalca, R. Ferragut, S. Aghion, A. Eilert, O. Diaz-Morales, C. Liu, A. L. Koh, T. W. Hansen, L. G. M. Pettersson and A. Nilsson, Nature and Distribution of Stable Subsurface Oxygen in Copper Electrodes During Electrochemical CO 2 Reduction, *J. Phys. Chem. C*, 2017, **121**, 25003–25009.

23 A. Eilert, F. Cavalca, F. S. Roberts, J. Osterwalder, C. Liu, M. Favaro, E. J. Crumlin, H. Ogasawara, D. Friebel, L. G. M. Pettersson and A. Nilsson, Subsurface Oxygen in Oxide-Derived Copper Electrocatalysts for Carbon Dioxide Reduction, *J. Phys. Chem. Lett.*, 2017, **8**, 285–290.

24 M. Fields, X. Hong, J. K. Nørskov and K. Chan, Role of Subsurface Oxygen on Cu Surfaces for CO 2 Electrochemical Reduction, *J. Phys. Chem. C*, 2018, **122**, 16209–16215.

25 C. Zhan, F. Dattila, C. Rettenmaier, A. Bergmann, S. Kühl, R. García-Muelas, N. López and B. R. Cuenya, Revealing the CO Coverage-Driven C-C Coupling Mechanism for Electrochemical CO2 Reduction on Cu2O Nanocubes *via Operando* Raman Spectroscopy, *ACS Catal.*, 2021, **11**, 7694–7701.

26 S. B. Scott, T. V. Hogg, A. T. Landers, T. Maagaard, E. Bertheussen, J. C. Lin, R. C. Davis, J. W. Beeman, D. Higgins, W. S. Drisdell, C. Hahn, A. Mehta, B. Seger, T. F. Jaramillo and I. Chorkendorff, Absence of Oxidized Phases in Cu under CO Reduction Conditions, *ACS Energy Lett.*, 2019, **4**, 803–804.

27 J.-J. Velasco-Vélez, T. Jones, D. Gao, E. Carbonio, R. Arrigo, C.-J. Hsu, Y.-C. Huang, C.-L. Dong, J.-M. Chen, J.-F. Lee, P. Strasser, B. Roldan Cuenya, R. Schlögl, A. Knop-Gericke and C.-H. Chuang, The Role of the Copper Oxidation State in the Electrocatalytic Reduction of CO 2 into Valuable Hydrocarbons, *ACS Sustainable Chem. Eng.*, 2019, **7**, 1485–1492.

28 H. S. Jeon, J. Timoshenko, C. Rettenmaier, A. Herzog, A. Yoon, S. W. Chee, S. Oener, U. Hejral, F. T. Haase and B. Roldan Cuenya, Selectivity Control of Cu Nanocrystals in a Gas-Fed Flow Cell through CO2 Pulsed Electroreduction, *J. Am. Chem. Soc.*, 2021, **143**, 7578–7587.

29 J. Timoshenko, A. Bergmann, C. Rettenmaier, A. Herzog, R. M. Arán-Ais, H. S. Jeon, F. T. Haase, U. Hejral, P. Grosse, S. Kühl, E. M. Davis, J. Tian, O. Magnussen and B. Roldan Cuenya, Steering the structure and selectivity of CO2 electroreduction catalysts by potential pulses, *Nat. Catal.*, 2022, **5**, 259–267.

30 A. Dutta, M. Rahaman, M. Mohos, A. Zanetti and P. Broekmann, Electrochemical CO 2 Conversion Using Skeleton (Sponge) Type of Cu Catalysts, *ACS Catal.*, 2017, **7**, 5431–5437.

31 A. J. Garza, A. T. Bell and M. Head-Gordon, Is Subsurface Oxygen Necessary for the Electrochemical Reduction of CO2 on Copper?, *J. Phys. Chem. Lett.*, 2018, **9**, 601–606.

32 P. Grosse, D. Gao, F. Scholten, I. Sinev, H. Mistry and B. Roldan Cuenya, Dynamic Changes in the Structure, Chemical State and Catalytic Selectivity of Cu Nanocubes during CO2 Electroreduction: Size and Support Effects, *Angew. Chem., Int. Ed.*, 2018, **57**, 6192–6197.

33 J. Timoshenko and B. Roldan Cuenya, In Situ/Operando Electrocatalyst Characterization by X-ray Absorption Spectroscopy, *Chem. Rev.*, 2021, **121**, 882–961.

34 S.-C. Lin, C.-C. Chang, S.-Y. Chiu, H.-T. Pai, T.-Y. Liao, C.-S. Hsu, W.-H. Chiang, M.-K. Tsai and H. M. Chen, Operando time-resolved X-ray absorption spectroscopy reveals the chemical nature enabling highly selective CO2 reduction, *Nat. Commun.*, 2020, **11**, 3525.

35 Y. Wang, A. Dutta, A. Iarchuk, C. Sun, S. Vesztergom and P. Broekmann, Boosting Nitrate to Ammonia Electroconversion through Hydrogen Gas Evolution over Cu-foam@mesh Catalysts, *ACS Catal.*, 2023, **13**, 8169–8182.
36 S. Jiang, K. Klingan, C. Pasquini and H. Dau, New aspects of operando Raman spectroscopy applied to electrochemical CO2 reduction on Cu foams, *J. Chem. Phys.*, 2019, **150**, 41718.
37 S. H. Lee, J. C. Lin, M. Farmand, A. T. Landers, J. T. Feaster, J. E. Avilés Acosta, J. W. Beeman, Y. Ye, J. Yano, A. Mehta, R. C. Davis, T. F. Jaramillo, C. Hahn and W. S. Drisdell, Oxidation State and Surface Reconstruction of Cu under CO2 Reduction Conditions from *In Situ* X-ray Characterization, *J. Am. Chem. Soc.*, 2021, **143**, 588–592.
38 H.-C. Shin and M. Liu, Copper Foam Structures with Highly Porous Nanostructured Walls, *Chem. Mater.*, 2004, **16**, 5460–5464.
39 H.-C. Shin, J. Dong and M. Liu, Porous Tin Oxides Prepared Using an Anodic Oxidation Process, *Adv. Mater.*, 2004, **16**, 237–240.
40 A. H. Clark, J. Imbao, R. Frahm and M. Nachtegaal, ProQEXAFS: a highly optimized parallelized rapid processing software for QEXAFS data, *J. Synchrotron Radiat.*, 2020, **27**, 551–557.
41 J. Rabeah, V. Briois, S. Adomeit, C. La Fontaine, U. Bentrup and A. Brückner, Multivariate Analysis of Coupled Operando EPR/XANES/EXAFS/UV-Vis/ATR-IR Spectroscopy: A New Dimension for Mechanistic Studies of Catalytic Gas-Liquid Phase Reactions, *Chem. - Eur. J.*, 2020, **26**, 7395–7404.
42 W. H. Cassinelli, L. Martins, A. R. Passos, S. H. Pulcinelli, C. V. Santilli, A. Rochet and V. Briois, Multivariate curve resolution analysis applied to time-resolved synchrotron X-ray Absorption Spectroscopy monitoring of the activation of copper alumina catalyst, *Catal. Today*, 2014, **229**, 114–122.
43 J. Jaumot, A. de Juan and R. Tauler, MCR-ALS GUI 2.0: New features and applications, *Chemom. Intell. Lab. Syst.*, 2015, **140**, 1–12.
44 B. Ravel and M. Newville, *ATHENA and ARTEMIS*, John Wiley & Sons, Ltd, 2020.
45 A. Merkys, A. Vaitkus, A. Grybauskas, A. Konovalovas, M. Quirós and S. Gražulis, Graph isomorphism-based algorithm for cross-checking chemical and crystallographic descriptions, *J. Cheminf.*, 2023, **15**, 25.
46 A. Vaitkus, A. Merkys and S. Gražulis, Validation of the Crystallography Open Database using the Crystallographic Information Framework, *J. Appl. Crystallogr.*, 2021, **54**, 661–672.
47 A. Vaitkus, A. Merkys, T. Sander, M. Quirós, P. A. Thiessen, E. E. Bolton and S. Gražulis, A workflow for deriving chemical entities from crystallographic data and its application to the Crystallography Open Database, *J. Cheminf.*, 2023, **15**, 123.
48 T. Binninger, E. Fabbri, A. Patru, M. Garganourakis, J. Han, D. F. Abbott, O. Sereda, R. Kötz, A. Menzel, M. Nachtegaal and T. J. Schmidt, Electrochemical Flow-Cell Setup for *In Situ* X-ray Investigations, *J. Electrochem. Soc.*, 2016, **163**, H906–H912.
49 A. Gaur, B. D. Shrivastava and S. K. Joshi, Copper K-edge XANES of Cu(I) and Cu(II) oxide mixtures, *J. Phys.: Conf. Ser.*, 2009, **190**, 12084.
50 C. Powell, X-ray Photoelectron Spectroscopy Database XPS,Version 4.1, NIST Standard Reference Database 20, 1989, accessed 20 December 2023.
51 J. A. Torres-Ochoa, D. Cabrera-German, O. Cortazar-Martinez, M. Bravo-Sanchez, G. Gomez-Sosa and A. Herrera-Gomez, Peak-fitting of Cu 2p photoemission spectra in Cu0, Cu1+, and Cu2+ oxides: A method for discriminating Cu0 from Cu1+, *Appl. Surf. Sci.*, 2023, **622**, 156960.
52 J. Kaur, A. Khanna, R. Kumar and R. Chandra, Growth and characterization of Cu2O and CuO thin films, *J. Mater. Sci.: Mater. Electron.*, 2022, **33**, 16154–16166.
53 L. Debbichi, M. C. Marco de Lucas, J. F. Pierson and P. Krüger, Vibrational Properties of CuO and Cu 4 O 3 from First-Principles Calculations, and Raman and Infrared Spectroscopy, *J. Phys. Chem. C*, 2012, **116**, 10232–10237.
54 K. Reimann and K. Syassen, Raman scattering and photoluminescence in Cu2O under hydrostatic pressure, *Phys. Rev. B: Condens. Matter Mater. Phys.*, 1989, **39**, 11113–11119.
55 M. Pourbaix, *Atlas of Electrochemical Equilibria in Aqueous Solutions*, Pergamon Press, Brussels, 1966.

